

# Microstructural Index to Quantify Thermal Spray Deposit Microstructures Using Image Analysis

G. Montavon, C. Coddet, C.C. Berndt, and S.-H. Leigh

(Submitted 21 March 1997; in revised form 13 October 1997)

The basic metallographic analysis leads to qualitative interpretation of the structural characteristics of a microstructure, for example the presence of phases, and the description of singularities such as inclusions. On the contrary, microstructural characterization which implements image analysis leads to a quantified analysis of structural characteristics. A method is described to assess thermal spray deposit microstructures using image analysis by means of a metallographic index. This index is based on the determination of several stereological and morphological parameters by primary reference to the size-shape distributions of the features, the fractal dimension of the deposit upper surface, and the Euclidean distance map of the bodies of interest. This work employs quantitative metallography on a much wider scale to provide better quality control of deposit microstructures.

**Keywords** Euclidean distance map, fractal dimension, image analysis, metallographic index, quantitative metallography, stereology

## 1. Introduction

In the materials science field, metallographic analyses are usually accomplished on cross sections because of the opacity of materials. Such metallographic examination is widely used as an analytical tool to characterize microstructures and leads to the qualitative and sometimes semiquantitative knowledge of physical and structural characteristics, such as the presence of a given phase, a typical component, and in the specific case of thermal spray deposits, the porosity level and the fraction of unmolten particles. Such information offers little specific quantitative information to fully describe the microstructure. Usually, the quality and acceptance for a given application of thermal spray deposits are assessed using a "pass or fail" criteria, which is based on several microstructural features, such as the porosity level and the oxide content, and are observed by inspection through a light reflected microscope (Ref 1). Sometimes, photographic standards (Ref 2, 3) are used for visual comparisons with the observed microstructures.

The image processing and image analysis of microstructures acquired using a charge coupled device (CCD) video camera can be very helpful in providing quantitative data on, for example, feature measurements. Such data could be used for better quality control of thermal spray processes and applications. This paper suggests the use of quantitative metallography on a much wider scale to improve quality control of deposit microstructures and defines a metallographic index which could be applied to any type of material deposited using a thermal spray process.

G. Montavon and C. Coddet, Laboratoire d'Études et de Recherches sur les Matériaux et les Propriétés de Surface, Institut Polytechnique de Sévenans, BP 449, 90 010 Belfort Cedex, France; C.C. Berndt, Center for Thermal Spray Research, State University of New York at Stony Brook, Stony Brook, NY 11755-2275, USA; and S.-H. Leigh, Research Institute of Industrial Science and Technology (RIST), Materials Research Division, #32 Hyoja-Dong, Nam-ku, Pohang City, 790-600 Kyungbuk, Korea. Contact e-mail: ghislain.montavon@utbm.fr.

tures and defines a metallographic index which could be applied to any type of material deposited using a thermal spray process.

## 2. Experimental Procedure

### 2.1 Specimens and Metallographic Preparations

Titanium powder (Stark No. 155.090 of +45–160  $\mu\text{m}$  typical particle size distribution) and copper powder (Amdry No. 3263 of +5–45  $\mu\text{m}$  typical particle size distribution) were plasma sprayed, using either atmospheric plasma spraying (APS) (for the titanium powder) or vacuum plasma spraying (VPS) conditions (for the copper powder), with a Plasma-Technik (Sulzer-Metco AG, Wohlen, Switzerland) F4 torch. For the titanium powder, the spray parameters were adjusted to produce very rugged deposit surfaces. In each case, the substrates were AISI 316 stainless steel coupons. Prior to spraying, they were cleaned, alcohol rinsed, and grit-blasted (6  $\mu\text{m}$  arithmetic average surface roughness). During spraying, APS specimens were cooled to ~373 K using air jets, while the VPS specimens were heated to ~923 K using a semitransferred arc. Both systems were selected as examples of different microstructures.

After spraying, the samples were cross sectioned using a diamond saw in an oil medium and mounted in epoxy rings before grinding and polishing. To study the spatial distributions of the bodies of interest (such as pores), nine cross-section angles, ranging from 90° (normal-to-the-deposit-surface angle) to 10° (for example, 90°, 80°, 70°, 60°, 50°, 40°, 30°, 20°, and 10°) were considered (Fig. 1). The metallographic preparation was identical for all deposits and consisted of grinding with P1200, P2400, and P4000 grade SiC papers, successively, followed by diamond slurry polishing using, in sequence, 6, 3, and 1  $\mu\text{m}$  sized media with ultrasonic rinsing between each step.

### 2.2 Image Analysis

Metallographic microstructures were observed on cross sections using an optical microscope, a CCD camera, and an image analysis system. Image analysis processing consisted of (a)

elimination from the original image of any artifacts or optical interferences and (b) clear identification of features of interest (for example, pores and phases). Figure 2 shows that image analysis can be divided into four successive steps: (a) the gray level image acquisition using a CCD camera, (b) the processing of this image, in view of eliminating all interferences and clearly identifying the bodies of interest, (c) the image analysis itself, which

consists of extracting numerical parameters relative to these bodies (size, shape, spatial distribution, etc.), and finally (d) the statistical analysis of the data by implementation of stereological protocols.

Since metallographic analyses are usually accomplished on cross sections because of the opacity of the microstructures, attention is drawn to the fact that an observation following a cross-

Nomenclature			
$a$	ellipsoid minor axis, $\mu\text{m}$	$q$	ellipse axial ratio, dimensionless
$A$	surface area, $\mu\text{m}^2$	$R_a$	average surface roughness, $\mu\text{m}$
$A_A$	surface area of the bodies of interest per unit of surface area, dimensionless	rms	root mean square surface roughness, $\mu\text{m}$
$b$	ellipsoid major axis, $\mu\text{m}$	Rsk	surface roughness skewness, dimensionless
$C(\tau)$	autocovariance function, surface descriptor	$s$	number of shape classes
$d$	Euclidean dimension, dimensionless integer	Sm	surface roughness mean peak spacing, $\mu\text{m}$
$D$	fractal dimension, dimensionless strictly noninteger	$V_V$	volume of bodies of interest per unit volume of aggregate, dimensionless
$i$	pixel calibration, $\mu\text{m}$	$x^2$	ellipsoid eccentricity, dimensionless
$k$	number of size classes, dimensionless integer	$y^2$	best fitting ellipse eccentricity, dimensionless
$k_0(q)$	the DeHoff shape factor for oblate particles, dimensionless	$Z$	the DeHoff intermediate coefficient, $\mu\text{m}^{-1}$
$L$	length, $\mu\text{m}$	$\beta_{i,j}$	the Saltykov factor, dimensionless
$L_T$	true length of the intercepted lines per field of view, $\mu\text{m}$	$\Delta$	increment of size class, dimensionless
$m$	best fitting ellipse minor axis, $\mu\text{m}$	$\epsilon$	overlapping circle radius, $\mu\text{m}$
$M$	best fitting ellipse major axis, $\mu\text{m}$	$\eta$	measuring element size, $\mu\text{m}$
$n_i$	number of ellipses per unit area of plane section in each size class, $\mu\text{m}^{-2}$	$\lambda$	mean free path, dimensionless
$N_A$	number of ellipses per unit area of plane section, $\mu\text{m}^{-2}$	$\mu$	average value
$N_i$	number of features intercepted per field of view, dimensionless integer	$\sigma$	standard deviation
$N_L$	number of intercepts per unit length of intercepted lines, $\mu\text{m}^{-1}$	<b>Acronyms</b>	
$N_V$	number of ellipsoidal particles per unit volume of aggregate, $\mu\text{m}^{-3}$	ACF	autocorrelation function (surface descriptor)
$(N_V)_i$	number of ellipsoidal particles per unit volume of aggregate in each size class, $\mu\text{m}^{-3}$	ANDED	added following the "AND" Boolean logic
		CCD	charge coupled device
		EDM	Euclidean distance map
		Ex-ORing	adding the complementary feature following the "OR" Boolean logic
		MS	Minkowski sausage
		PSD	power spectral density (surface descriptor)
		WIP	water immersion porosimetry

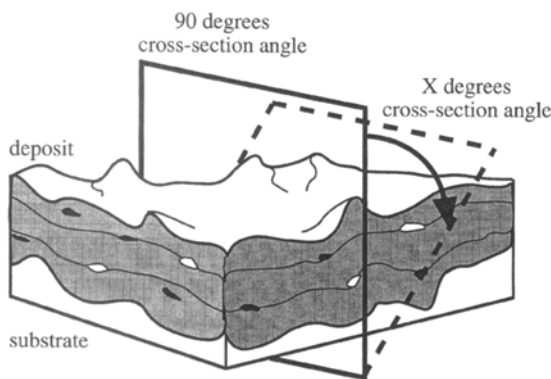


**Fig. 1** Schematic of the cross-section angles used to study the spatial distributions of the bodies of interest

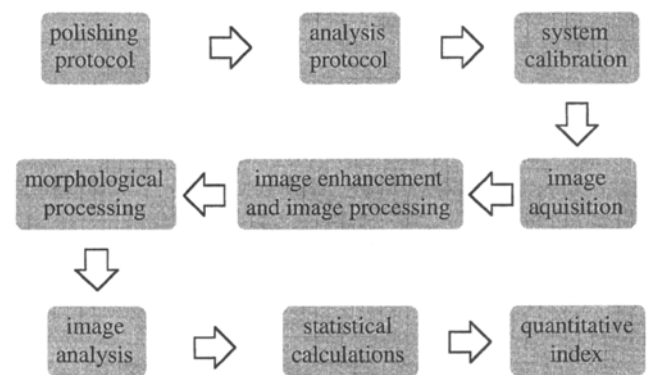


**Fig. 2** Schematic of the steps implemented to achieve quantitative metallography

sectioned plane does not necessarily reflect the entire three-dimensional microstructure but only the intersection of the structure with this specific plane. As illustrated in Fig. 3, a cavernous body sectioned on three different test planes may exhibit three different morphologies, and two different bodies cut following a single test plane might exhibit very similar morphologies. In such conditions, results deduced from such observations have to be analyzed with respect to an appropriate perception.

Bias and errors can also be introduced in the results from image analysis. The ASTM E 1382-91 standard (Ref 4) lists the major induced interferences. They are relative to the surface preparation before analysis and to the image analysis itself. The major possible biases are:

- An improper polishing technique that leaves scratches on the surface or produces pullouts and other defects.
- Etching techniques that produce only partial delineation of the body boundaries.
- The selection of test areas that are not representative of the entire microstructure, especially for oriented (for example, anisotropic) microstructures.
- The detection of artificial features generated by the image analysis system (generally due to an excess of contrast or to several gray levels in the same body) or the lack of detection of real boundaries (generally due to poor contrast or to the use of an inappropriate etching technique).
- The presence of dust in the microscope, in the camera system, or on the examined field.
- A nonuniform illumination of the sample, which influences the feature detection.

Calibration of the image analysis system is the first step in quantitative analysis. This calibration permits correlation of the pixel area with respect to physical dimensions. Practically, the calibration is accomplished by defining the distance between two noncontinuous pixels. This operation is performed from a digital image of a calibrated scale, digitized following the same rules as those to acquire the digital images of the microstructures to be analyzed.

In this work, image analyses were carried out on a Power Macintosh 7200/90 computer using the public domain NIH 1.59 program (developed at the U.S. National Institutes of Health and available through Internet by anonymous FTP from [zippy.nimh.nih.gov](http://zippy.nimh.nih.gov) or on floppy disk from the National Technical Information Service, Springfield, Virginia, part number PB95-500195GE1).

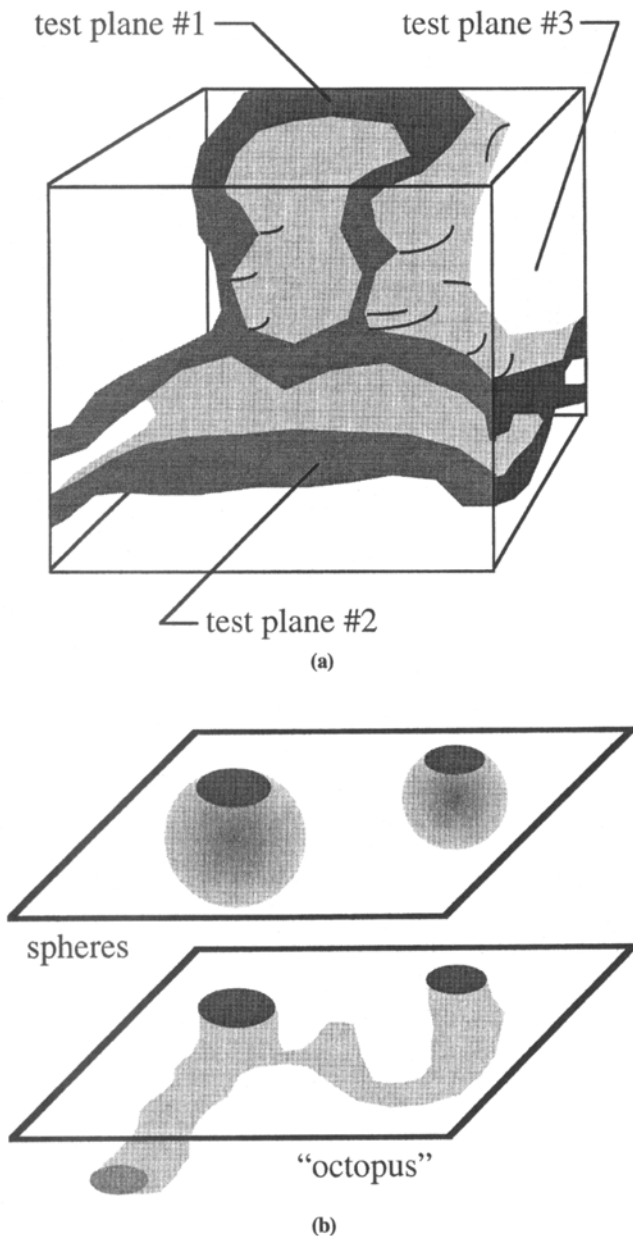


**Fig. 3** Schematic of possible misperceptions in metallography. (a) Same body cut following three different test planes and exhibiting three different morphologies. (b) Two different bodies cut following the same test plane and exhibiting the same morphologies

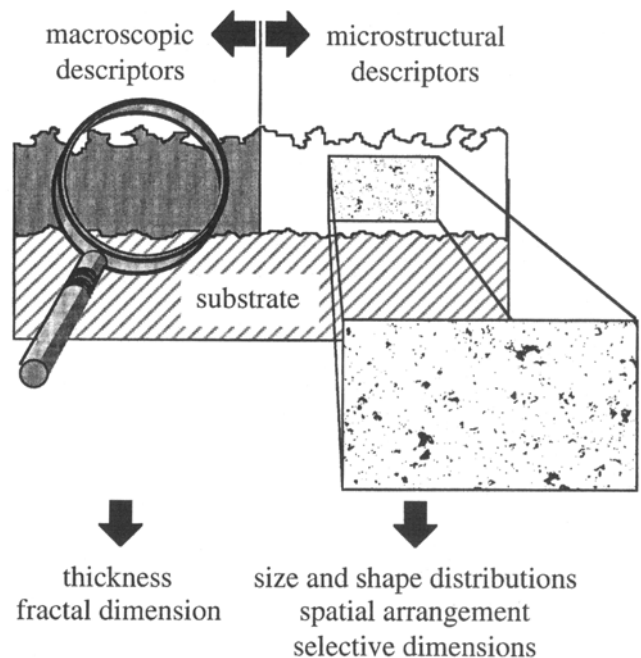
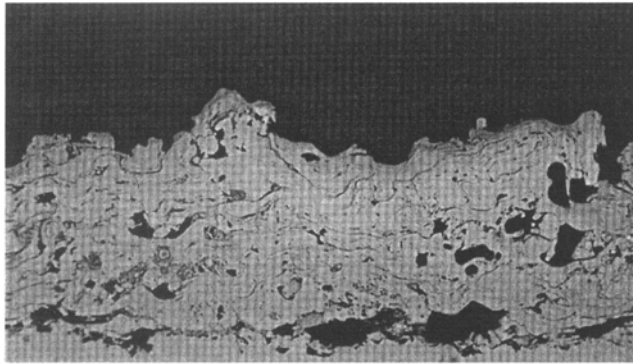


**Fig. 4** Macroscopic and microstructural descriptors constituting the metallographic index

### 3. Definition of the Metallographic Index

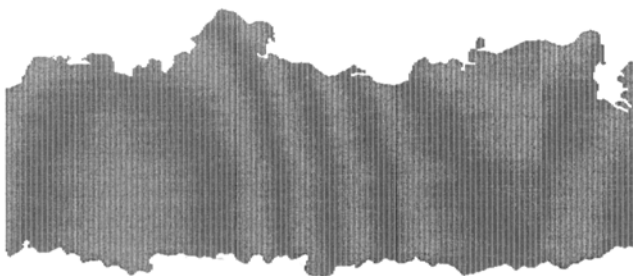
Quantitative metallography is based on the fact that for many microstructures it is possible to determine average values and distributions of these values referring to the major components constituting a deposit; for example, grains, flattened particles,



(a)



(b)



(c)

**Fig. 5** Schematic of the image processing implemented to determine a deposit average thickness. (a) Gray level image of a cross section perpendicular to the surface of a rugged titanium deposit. (b) Binary image of the deposit profile. (c) Processed image resulting from the ANDing of a mask with (b)

unmolten particles, porosity, and oxides. The suggested metallographic index is constituted by macroscopic (such as overall size and shape) and microstructural (that is, size, shape, and spatial distribution) descriptors, as schematically displayed in Fig. 4. The macroscopic descriptors refer to the global analysis of a deposit cross section, mainly through its average thickness and its surface ruggedness by fractal dimensions. The microstructural descriptors refer to the analysis of the deposit components through their size and shape distributions by stereological analysis and through their spatial distribution by Euclidean distances. In the following, for each descriptor of the metallographic index, a brief description of the theoretical background is given, followed by an illustrative example based on the two considered thermal spray deposit microstructures.

### 4. Macroscopic Descriptors

#### 4.1 Deposit Average Thickness

The thickness is, among the various characteristics of a thermal spray deposit, an important factor in the deposit service performance and is always exactly specified. Moreover, the deposit thickness derives directly from the apparent deposition efficiency of the application process. Several destructive (Ref 5) and nondestructive (Ref 6) standards provide methods to measure deposit thicknesses. The ASTM B 487-85 standard (destructive method) requires the use of a stage graticule eyepiece superimposed on the image of a cross section of the deposit, observed at low magnification (for example, 2 $\times$  or 3 $\times$ ). Such an approach is based on the human operator perception of the deposit profile and is only suitable for acceptance testing. The deposit average thickness descriptor, determined using image analysis, permits a more appropriate and precise calculation of the deposit thickness.

The first step in image processing is extracting the contours of the deposit from the initial gray level image of a deposit cross section (for example, lower and upper surfaces). The magnification of the microscope has to be adapted to the thickness of the sample to be analyzed. The second step consists in superimposing on the binary deposit profile a mask formed by parallel and equidistant lines, in such a way that the lines are perpendicular to the deposit/substrate interface. Finally, the image of the mask is "ANDed," (that is, added following the AND Boolean logic), to the image of the deposit profile, as illustrated in Fig. 5. The image analysis is now simply performed by counting the total length of the intercepted lines (the resulting image shows only segments of lines which cross the deposit profile) as well as the number of intercepted lines. The data representative of the anchor effects (for example, cavities at the deposit surface) are deleted to adjust the raw data (these values are very low compared to the values representative of the bulk deposit) and are not considered in the calculation of the thickness, see Fig. 6. Finally, the average coating thickness is determined by dividing the total lengths of the adjusted data by the adjusted number of lines. Several fields of view of the same deposit have to be analyzed using this protocol to determine a representative value of the deposit average thickness; a number of five fields of view seems reasonable.

This protocol was applied to a rough titanium deposit where five fields of view of approximately 500  $\mu\text{m}$  width by 300  $\mu\text{m}$  height were processed. Figure 5(a) illustrates one of the processed fields. The mask consisted of one pixel (for example, 0.96  $\mu\text{m}$  at the 112 $\times$  used magnification) width lines at 1  $\mu\text{m}$  interval; see Fig. 5(b). The average thickness, measured over  $\sim 2.5$  mm, was 228  $\mu\text{m}$  with a standard deviation of 8  $\mu\text{m}$ . Even though the deposit upper surface was very rugged and the anchor effects were particularly emphasized, the low value of the standard deviation indicates a homogeneous deposit thickness. This is confirmed by the high value ( $m = 10.5$ ) of the Weibull modulus (Ref 7) relative to the data representative of the deposit thickness (Fig. 7) which reflects a small variability in the data. A degree of undercut can be determined from the data representative of the anchor effect. It is defined as the average value of the aforementioned data. On the presented example, the degree of undercut is equal to 13.3  $\mu\text{m}$  with a standard deviation of 12.8  $\mu\text{m}$  (that is,  $\sigma/\mu = 0.96$ ). The high variability in the data representative of the anchor effect is demonstrated through the particularly low value of the corresponding Weibull modulus: 1.2.

#### 4.2 Deposit Fractal Dimension

The chemical and physical properties of thermal spray deposits depend partially on surface characteristics such as texture and roughness. For example, the corrosion resistance of a deposit changes with the surface characteristics since the real surface area differs from the apparent surface area (Ref 8-10). A second example is the heat flux transmitted through a deposit which depends on the real coupling surface (Ref 11). The geometric characteristics of a surface are commonly defined using surface parameters and statistical functions. The surface parameters are usually classified as height parameters (for example,  $R_a$  and rms roughness), wavelength parameters (for

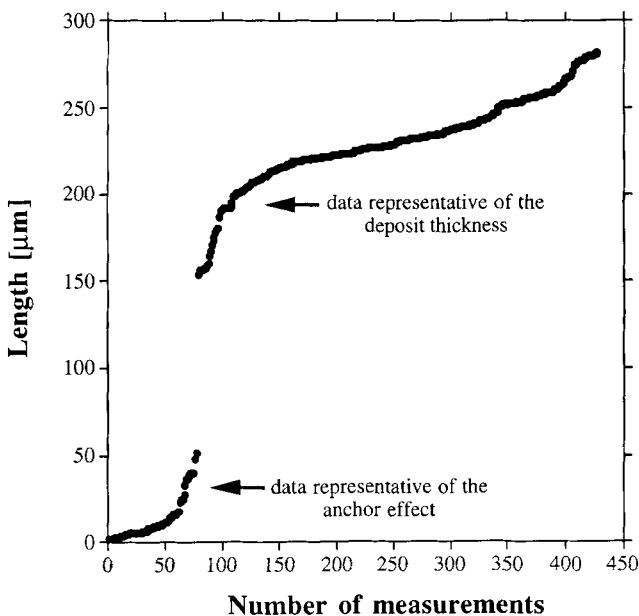


**Fig. 6** Distribution of the length measurements performed on a deposit cross section to determine its average thickness, displaying the data representative of the anchor effect and the data representative of the deposit thickness itself

example,  $S_m$ ), shape parameters (for example,  $R_{sk}$ ), and hybrid parameters resulting from combinations of the aforementioned surface parameters. The statistical functions used as descriptors for a surface texture yield knowledge of the surface geometry. They refer mainly to the power spectral density (PSD), the autocovariance function,  $C(\tau)$ , and the autocorrelation function (ACF). However, the use of such descriptors is not complete when the surface ruggedness becomes important, for example when the roughness of the deposit is high, when the scale of the roughness becomes much lower than the size of the sensor, or when the anchor effect is emphasized, as illustrated in Fig. 8. In such cases, the bias resulting from the measurements becomes too important, and the description ceases to be representative of the topology of the surface. The determination of the deposit upper surface fractal dimension can circumvent such a difficulty

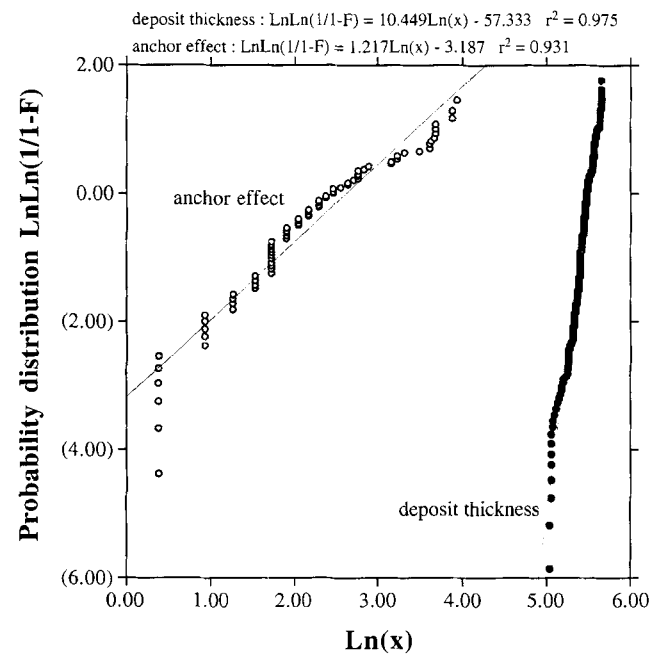


**Fig. 7** Weibull plot of data representative of the deposit thickness and the anchor effect presented in Fig. 6

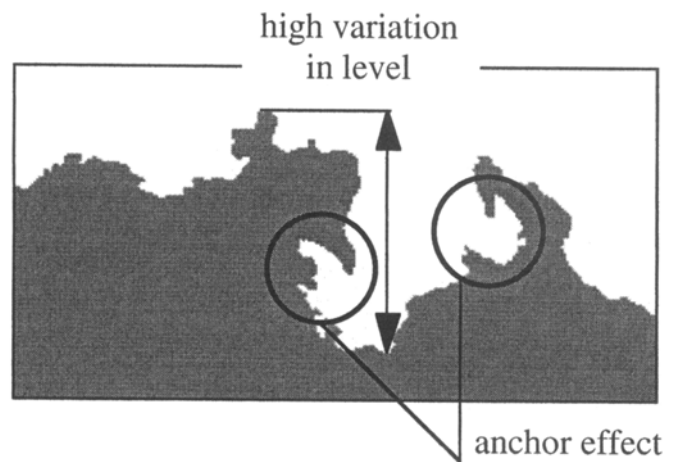


**Fig. 8** Schematic of the rough upper surface of a thermal spray deposit, showing the anchor effect

(especially when the anchor effect is emphasized) or can appear as a complementary index to the commonly used roughness parameters.

Almost all geometric forms used to describe objects refer to Euclidean geometry, such as lines, planes, arcs, cylinders, and spheres. These elements are classified as belonging to an integer dimension,  $d$ , either 1, 2, or 3. There are, however, many shapes which do not conform to the integer idea of dimension. In such cases, their perimeter dimension for example, increases as the measurement scale decreases, and a fractal analysis can be used (Ref 12). The notion of fractal dimension,  $D$ , provides a tool to quantify the ruggedness of profiles. For example, while a Euclidean line has a dimension of one, a fractal curve exhibits a dimension ranging from one to two, depending on the ruggedness of the curve. The fractal dimension can be obtained mathematically by iterative processes such as the Julia set (Ref 13), or they can be observed on real components, for example, natural fractals such as fern trees. The fractal geometry is based on the statistical self-similarity concept, which implies that a similar surface topology appears in a wide range of magnifications. The most significant difference between fractals obtained by a mathematical iterative process and fractals observed on real microstructures is the cutoffs at the lower and upper size scales for the real microstructure, for example, the atomic spacing for the

lower end (Ref 14). Fractal geometry has found a wide range of applicability in describing highly irregular surfaces or profiles (Ref 15-17).

The fractal dimension of Hausdorff-Besicovitch (content dimension) of a profile is defined (Ref 12):

$$D = 1 - \frac{\log L - \log L_0}{\log \eta} \quad (\text{Eq 1})$$

where  $L$  is the profile length,  $\eta$  is the measuring element size (for example, resolution), and  $L_0$  is a constant. The estimated length of the profile varies proportionally to the measuring element according to a power relationship.

The fractal dimension of Bouligand-Minkowski (overlapping dimension) of a profile is defined (Ref 12):

$$D = \lim_{\epsilon \rightarrow \infty} \left( 2 - \frac{\log A(\epsilon)}{\log \epsilon} \right) \quad (\text{Eq 2})$$

where  $\epsilon$  is the radius of the overlapping circle and  $A(\epsilon)$  is the area of the Minkowski sausage (MS) for a given overlapping. It is obvious that the area of the MS is accordingly higher than the circle radius (and hence the circle area) is high.

Two techniques may be used to determine the fractal dimension of a profile: the Mandelbrot-Richardson protocol leading to the calculation of the Hausdorff-Besicovitch fractal dimension (Ref 18) and the Bouligand-Minkowski protocol leading to the determination of the Minkowski fractal dimension (Ref 19). The dimensions provided by both methods may be different (Ref 20), and therefore, it is crucial to compare values obtained

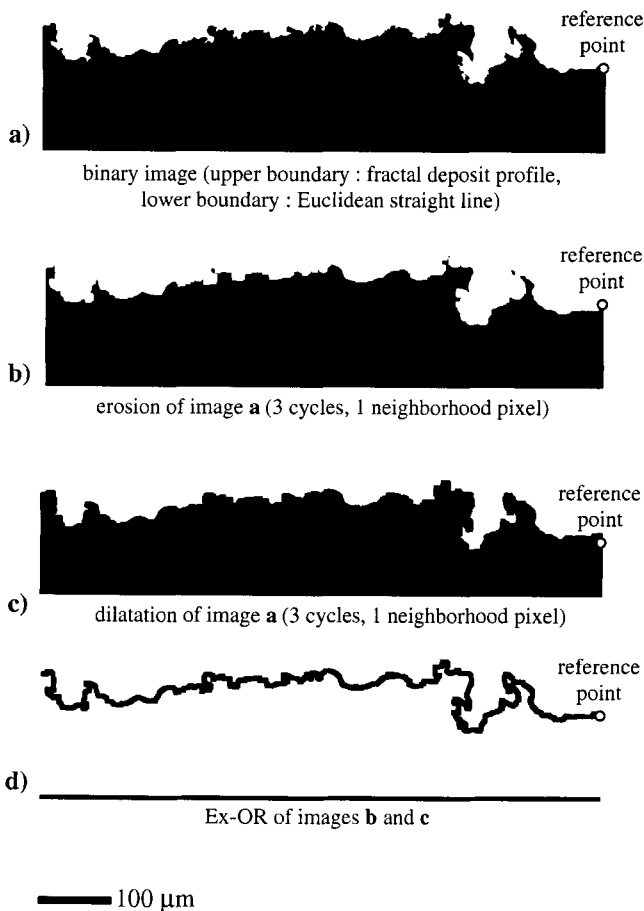


**Fig. 9** Schematic of the image processing implemented to determine the fractal dimension of a rugged deposit surface profile, using the Minkowski sausage method

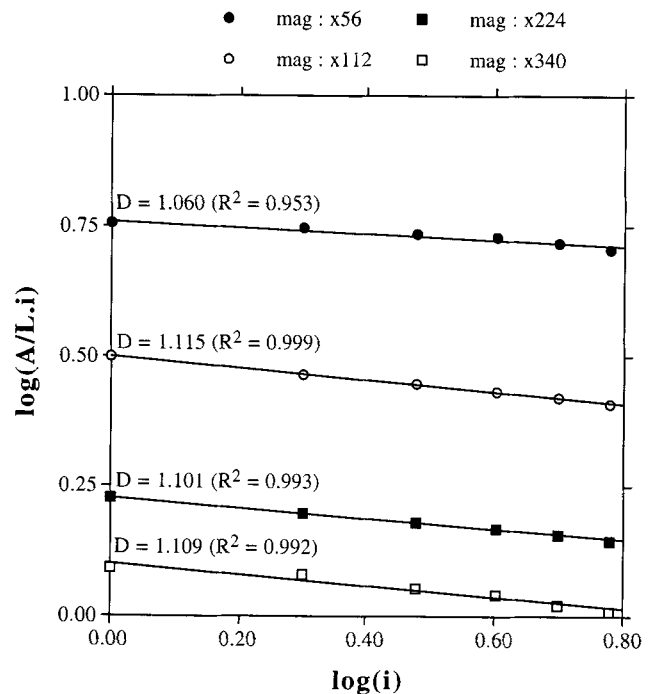


**Fig. 10** Plot of the log of the effective width of the boundary (area of Ex-OR divided by the length and the number of cycles; see Fig. 9) as a function of the number of cycles of the same location of a titanium deposit surface for several magnifications (the data in parentheses represent the correlation factors of the data fittings)

with the same protocol. The Hausdorff-Besicovitch fractal dimension is obtained from the direct measurement of a profile length at several magnifications. Then, the evolution of the profile length,  $L$ , is plotted with respect to the measuring element size (Mandelbrot-Richardson plot) on a log-log scale. The slope of the linear curve is equal to one minus the Hausdorff-Besicovitch fractal dimension of the profile (i.e.,  $1 - D$ ).

Due to its mathematical definition, the Bouligand-Minkowski fractal dimension can be obtained by an iterative erosion and dilation image processing (Ref 19, 21). By dilating successively (iterative cycles) at different depths (interface thickness) a selected region of a digital image and "EX-ORing" (that is, adding the complementary feature following the "OR" Boolean logic) the result with another image formed by eroding at the same depth the same region, pixels along the boundary defined an interface width, as illustrated in Fig. 9. In the second step of the procedure, the effective width of the boundary (equal to the area,  $A$ , divided by the length,  $L$ , and the number of iterative cycles,  $i$ ) is plotted versus the number of cycles,  $i$ , on a log-log scale. The slope of the linear curve thus obtained represents the Minkowski fractal dimension of the surface profile.

To establish the fractal character of a given microstructure, Hombogen (Ref 14) recommends that the following steps be assessed: (a) verification of the self-similarity concept, (b) determination of the upper and lower limits of the self-similarity, and (c) determination of the fractal dimension itself.

The MS protocol was applied to the rough titanium deposits, since a normal cross section of a deposit provides a profile which can be analyzed. First, to verify the self-similarity concept, the fractal dimension of one profile was calculated at several magnifications (that is, 56 $\times$ , 112 $\times$ , 224 $\times$ , and 340 $\times$ ); see Fig. 10. The fractal dimension changes from 1.060 at the 56 $\times$  magnification

to 1.109 at the 340 $\times$  magnification, indicating a reasonable self-similarity of the deposit surface (the smallest dimension differing from the highest only by  $\sim 5\%$ ), and hence its fractal character, in the scanned magnification range. Second, several fields of the same deposit were observed at the same magnification (that is, 112 $\times$ ), and their fractal dimension was determined, as illustrated in Fig. 11. The resulting dimensions are very close, ranging from 1.095 for the lowest to 1.115 for the highest, indicating that the selected fields of view were appropriate for the analysis. Finally, the fractal dimensions of the surface profile of several rough titanium deposits of different thicknesses (that is, from approximately 20 to 118  $\mu\text{m}$ ) were determined at a 112 $\times$  magnification, as illustrated in Fig. 12. Figure 13 compares the evolution of both the fractal dimension,  $D$ , and the average surface roughness,  $R_a$ , as a function of the deposit thickness. The same trend between the two descriptors is observed. The ruggedness of the profile is very close to the grit blasted substrate at the very beginning of the deposit building process (that is, sample No. 1) and significantly increases to reach a constant value for higher thicknesses, indicating that the deposit roughness results more from the choice of the spray parameters (for example, powder particle size distribution, thermal conductivity, and velocity of the plasma jet) than from the initial substrate roughness.

- sample #1, thickness = 31.39  $\mu\text{m}$ ,  $D = 1.061$  ( $R^2 = 0.993$ )    ●
- sample #2, thickness = 62.78  $\mu\text{m}$ ,  $D = 1.122$  ( $R^2 = 0.992$ )    ○
- sample #3, thickness = 94.17  $\mu\text{m}$ ,  $D = 1.133$  ( $R^2 = 0.985$ )    ■
- sample #4, thickness = 125.56  $\mu\text{m}$ ,  $D = 1.110$  ( $R^2 = 0.993$ )    □
- sample #5, thickness = 156.95  $\mu\text{m}$ ,  $D = 1.119$  ( $R^2 = 1.000$ )    ▲
- sample #6, thickness = 188.35  $\mu\text{m}$ ,  $D = 1.114$  ( $R^2 = 0.999$ )    △

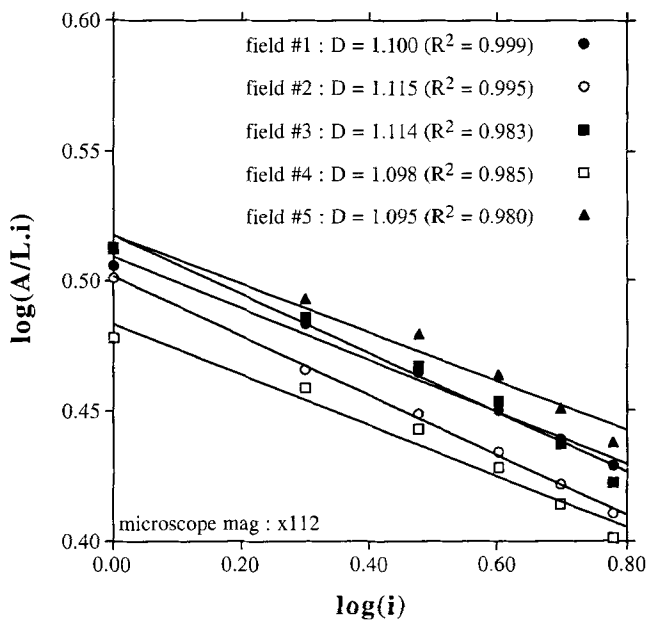


**Fig. 11** Plot of the log of the effective width of the boundary (area of Ex-OR divided by the length and the number of cycles; see Fig. 9) as a function of the number of cycles of different locations of a titanium deposit surface for the same magnification (the data in parentheses represent the correlation factors of the data fittings)

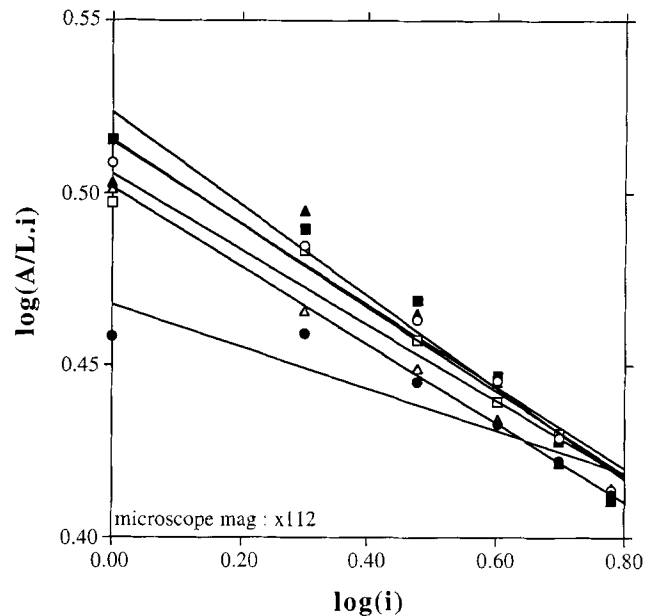


**Fig. 12** Plot of the log of the effective width of the boundary (area of Ex-OR divided by the length and the number of cycles; see Fig. 9) as a function of the number of cycles of surfaces of titanium deposits exhibiting increasing thicknesses (for example, from sample No. 1 to sample No. 6) for the same magnification (the data in parentheses represent the correlation factors of the data fittings)

## 5. Microstructural Descriptors

### 5.1 Size and Shape Distributions of the Bodies of Interest

The size and shape distributions of microstructural features are of great importance in the quantitative description of these microstructures, which in turn may explain the relationships between the process and the mechanical or other properties of thermal spray deposits (Ref 22, 23). These distributions can be determined by stereological analysis. Stereology, *stricto sensu*, deals with estimates for describing a three-dimensional space, when only two-dimensional sections through this space are

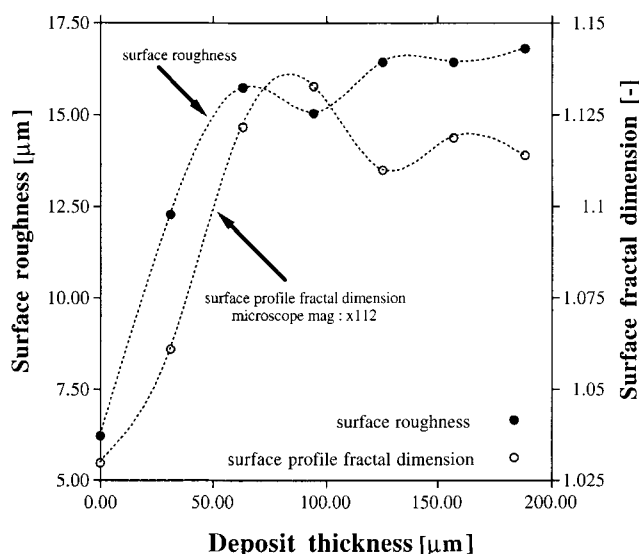


**Fig. 13** Plot of the evolution of the surface profile fractal dimension and average surface roughness of titanium deposits, as a function of their thickness

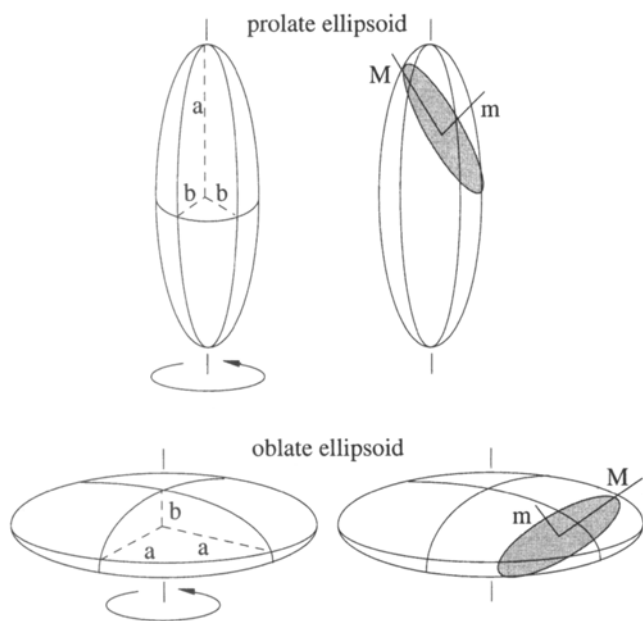


**Fig. 14** Schematic of prolate and oblate ellipsoidal shapes

available. It attempts to numerically characterize features of two-dimensional sections and to establish relationships with those features in a three-dimensional space (Ref 24). The rules of these estimates are based on geometric probabilities. The volume of an individual feature is not exactly determined, but the size and shape distributions of many objects are described (Ref 19). Many of the shapes encountered in metallurgical structures (for example, grains and inclusions) and especially in thermal spray deposits (for example, embedded particles, splats, and pores) can be approximated by spheroids, that is, ellipsoids of revolution (Ref 25). These spheroids result from the rotation of generating ellipses around an axis. Two basic morphologies can be considered, the prolate particle and the oblate particle, respectively, generated by rotation around the major axis,  $a$ , and around the minor axis,  $b$ , of an ellipse, as illustrated in Fig. 14. The intersection of such bodies with a test plane generates ellipses, characterized by their major axis,  $M$ , and their minor axis,  $m$ . Two protocols, among others (Ref 26, 27), allow a good description of the size-shape distributions of the spheroidal bodies embedded within an agglomerate, namely the protocols of DeHoff (Ref 28, 29) and Cruz-Orive (Ref 30-31). These protocols and some examples of their application to thermal spray deposits were previously presented (Ref 32-33), and therefore only a brief overview is given.

The DeHoff protocol, derived from the Schwartz-Saltykov analysis (Ref 34) for spherical particles, aims to obtain the size distribution of ellipsoidal particles within an aggregate. This protocol deals with systems of particles that consist of either prolate or oblate ellipsoids of revolution of the same axial ratio,  $q$  (that is, the particle shapes are considered to be constant within each size class). For prolate ellipsoids, the main dimension of interest is the major axis of the ellipse,  $M$ , in the polished plane, while in a system of oblate ellipsoids, it is the minor axis of the ellipse,  $m$ . The expression for the number of ellipsoid particles in each size class per volume unit of the aggregate is given:

$$(N_V)_j = \frac{1}{k(q) \cdot \Delta} \sum_{i=j}^{i=k} \beta(i,j) \cdot (N_A)_i \quad (\text{Eq 3})$$

where  $k(q)$  represents  $k_p(q)$  or  $k_o(q)$ , the shape factors for prolate or oblate spheroids, respectively,  $\Delta$  is the size increment,  $\beta(i,j)$  are the Saltykov coefficients, determined from the Saltykov matrix, and  $(N_A)_i$  is the number of ellipses of  $q$  axial ratio per unit area of the test plane in each size class. The shape factor for oblate particles is expressed:

$$k_o(q) = \int_0^{\pi/2} \int_0^{\pi/2} \frac{\sqrt{1 + (q^2 - 1) \cos^2 \phi} \sin \phi}{\pi/2} d\phi d\theta \quad (\text{Eq 4})$$

where  $\phi$  is the angle between the normal to the test plane (that is, polished plane) and the  $z$  axis, and  $\theta$  is the angle between the projection of this normal on the  $xy$  plane and the  $x$  axis, with respect to a standard Cartesian coordinate system. The total number of ellipsoidal particles in the aggregate is equal to:

$$N_V = \frac{2 \cdot (N_V)_i \cdot Z}{\pi \cdot q \cdot k(q)^2} \quad (\text{Eq 5})$$



where the intermediate coefficient  $Z$  is expressed:

$$Z = \frac{\pi \cdot q \cdot k(q)}{2 \cdot m_{\max}} \quad (\text{Eq 6})$$

The average axial ratio,  $q$ , of the measured ellipses, is then equal to:

$$q = \frac{\bar{m}}{\bar{M}} \quad (\text{Eq 7})$$

where  $\bar{m}$  and  $\bar{M}$  successively represent the average minor axis and the average major axis of the selected distribution of ellipses. The increment of size class,  $\Delta$ , is determined:

$$\Delta = \frac{m_{\max}}{k} \quad (\text{Eq 8})$$

where  $m_{\max}$  is the highest best fitting ellipse minor axis in the largest size class.

The general spheroid problem was solved by Cruz-Orive. He considered systems of particles consisting of either prolate or oblate ellipsoids of revolution of variable sizes (for example, size factors  $a$  or  $b$ , for prolate and oblate particles, respectively) with variable shapes, eccentricity  $x^2 = 1 - (a/b)^2$ .

Cruz-Orive established relationships between the ellipsoid size shape distribution,  $a$  or  $b$ ,  $x^2$  and the ellipse size shape distribution,  $m$  or  $M$ ,  $y^2 = 1 - (m/M)^2$  and obtained an expression for the number of spheroids in each class interval per volume unit of aggregate:

$$N_V(i,j) = \Delta^{-1} \sum_{i=1}^{i=s} \sum_{j=1}^{j=k} p^{ir} \cdot N_A(r,s) \cdot q^{sj} \quad (\text{Eq 9})$$

where  $\Delta$  is the size increment,  $N_A(r,s)$  is the number of ellipses of  $r$  shape class and  $s$  size class, and  $p^{ir}$  and  $q^{sj}$  are the size and shape coefficients, respectively. The bivariate distribution of ellipsoidal particles in an aggregate,  $N_V$ , can be expressed by the following relationship:

$$N_V = P^{-1} \cdot N_A \cdot Q^{-1} \quad (\text{Eq 10})$$

where  $P$  is a size matrix and  $Q$  is a shape matrix. The coefficients can be found in Ref 31.

The number of size classes,  $k$ , is chosen usually between 10 and 15, as well as the number of shape classes,  $s$ . The increment of size class,  $\Delta$ , is determined:

$$\Delta = \frac{M_{\max}}{k} \quad (\text{Eq 11})$$

where  $M_{\max}$  is the highest best fitting ellipse major axis in the largest class size.

To illustrate the use of stereological protocols, the porosity size distribution of a copper deposit was determined by implementing the DeHoff protocol for several cross-section angles. For each cross-section angle, four fields of view were randomly selected at a 112 $\times$  magnification. The image processing consisted of applying morphological filters to extract the porosity contours. The image analysis consisted of measurements of the

surface area and of the two best fitting ellipse axes, that is, minor and major axes, for each extracted void. Then, the raw data, representing typically about 700 porosity features were adjusted by subtracting the smallest and the highest values (area) at a level of 2.5% of the total values in order to discriminate against atypical data. Finally, the adjusted data were processed with the DeHoff protocol. Figure 15 illustrates the evolution of the number of voids per volume unit of aggregate as a function of the class size descriptor (best fitting ellipse minor axis). The same trend is observed for each cross-section angle: the number of small voids is greater than that of larger ones. The knowledge of the number of voids per unit volume of aggregate and class size, as well as that of the volume of porosity class size permits the calculation of the total volume of porosities per unit volume of the aggregate (that is,  $V_V$  ratio), as illustrated in Fig. 16, which displays the case of the 10 $^\circ$  cross-section angle. This distribution is typical of the size distribution of voids embedded within a thermal spray deposit (Ref 35, 36). It exhibits a bimodal shape, the first peak being representative of small voids of approximately 2 to 3  $\mu\text{m}$  diameter and the second one relative to large voids of approximately 7 to 8  $\mu\text{m}$  diameter. The porosity levels were determined for each cross-section angle by summation of the volumes of porosities per unit volume of the aggregate; results are given in Fig. 17 where the circles represent the average values of the four fields of view and the error bars are the corresponding standard deviations. The full line represents the average of the averages, whereas the dotted lines are the standard deviation associated with this calculated average. Figure 18 displays the evolution of the  $\sigma/\mu$  ratio of the porosity level as a function of the cross-section angle. No clear trend appears from this evolution, indicating that the accuracy of the results do not depend on the cross-section angle.

Another analysis evaluated the porosity levels (calculated  $V_V$  ratio) by implementing the DeHoff protocol and compared the results with those deduced from (a) the Delesse principle (Ref 37) (measured  $A_A$  ratio) applied on the binary images (the vol-

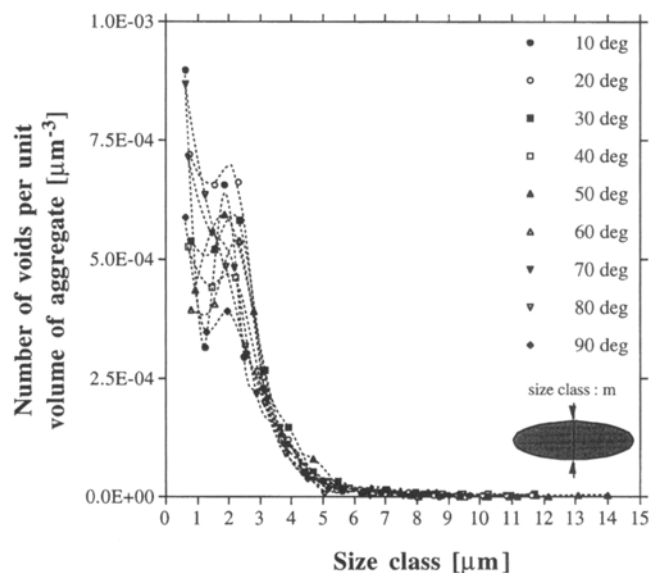


**Fig. 15** Evolution of the number of pores per unit volume of aggregate, as a function of the class size, determined with the DeHoff protocol, for different cross-section angles

ume of bodies of interest embedded within an aggregate per volume unit of aggregate is equal to the surface area of these same bodies per surface unit), and (b) water immersion porosimetry (WIP) (Ref 38) (measured  $V_V$  ratio).

The amount of f porosity of a polished sample was measured by implementing WIP, the measurements being carried out at 293 K in water with an additive to increase the surface wettability; see Fig. 19. The porosity levels deduced from the Delesse principle differ by 5 to 8% from the porosity levels obtained from the DeHoff principle. The difference between the porosity level determined using the DeHoff stereological protocol and the porosity level deduced from WIP is more important, ranging from 5% for the lowest difference (at a 70° cross-section angle) to 17% for the highest (at a 50° cross-section angle). These differences arise due to (a) the limitation of the DeHoff protocol, that is, the shape of the bodies of interest remains constant within each size class and (b) from the WIP limitation since open porosity is not fully considered. The implementation of the Cruz-Orive analysis generally leads to a better estimation of the porosity shape distributions, but it is more complex to apply. In the case of the DeHoff analysis, the combination of several cross-section angles reduces the data scattering so that reasonable values can be obtained.

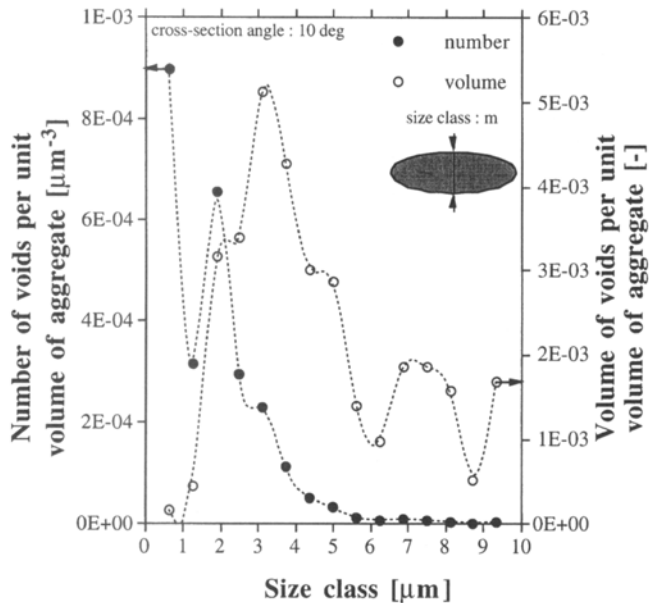


**Fig. 16** Evolution of the number and of the volume of pores per unit volume of aggregate, as a function of the class size, determined with the DeHoff protocol, for a 10° cross-section angle

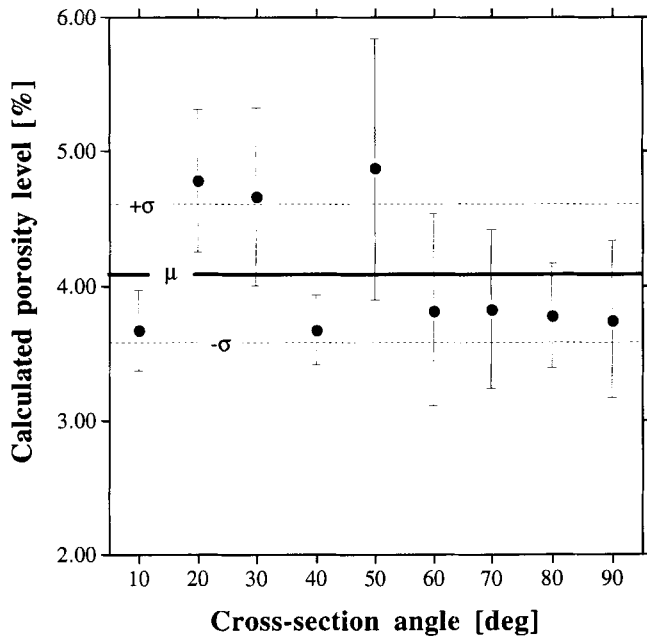


**Fig. 17** Calculated porosity level as a function of the cross-section angle, determined with the DeHoff protocol (average values and standard deviations represented by error bars). The  $\mu$  line represents the average of the calculated averages,  $-\sigma$  and  $+\sigma$  lines, the associated standard deviation

ity; see Fig. 19. The porosity levels deduced from the Delesse principle differ by 5 to 8% from the porosity levels obtained from the DeHoff principle. The difference between the porosity level determined using the DeHoff stereological protocol and the porosity level deduced from WIP is more important, ranging from 5% for the lowest difference (at a 70° cross-section angle) to 17% for the highest (at a 50° cross-section angle). These differences arise due to (a) the limitation of the DeHoff protocol, that is, the shape of the bodies of interest remains constant within each size class and (b) from the WIP limitation since open porosity is not fully considered. The implementation of the Cruz-Orive analysis generally leads to a better estimation of the porosity shape distributions, but it is more complex to apply. In the case of the DeHoff analysis, the combination of several cross-section angles reduces the data scattering so that reasonable values can be obtained.

## 5.2 Degree of Clustering of the Bodies of Interest

Several properties of thermal spray deposits depend on the spatial distribution of the phases and porosity. For example, tensile properties depend on the degree of clustering of the pores since highly clustered porosity generates regions of poor mechanical properties where cracks easily propagate through the entire volume. Another example is thermal conductivity where the thermal flux through the deposit thickness is related to the spatial distribution of the pores within the microstructure (Ref 11, 39). A further example is the spatial distribution of the crystalline phases within hydroxyapatite or other calcium phosphate biomedical deposits since the solubility depends on the degree of crystallinity of the coating (Ref 40, 41). The degree of clustering of the bodies of interest (pores, specific phases) can be quantified using Euclidean distance indices. These indices derive from Euclidean distance maps (EDM) Ref 19).

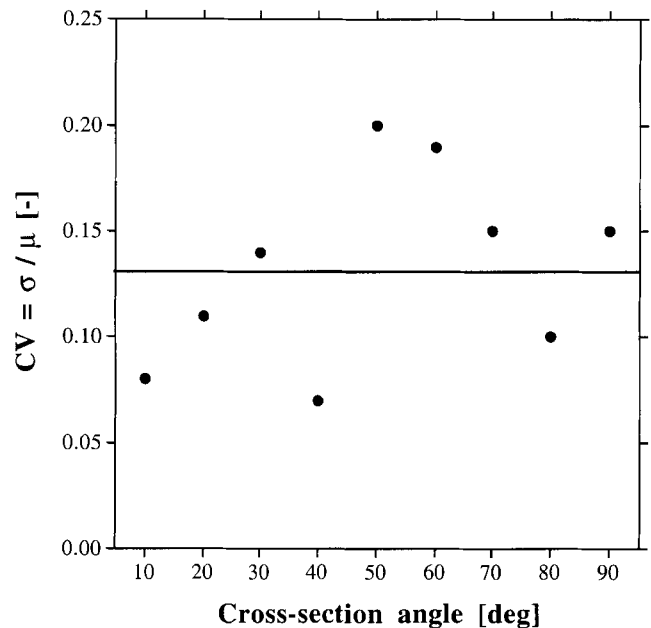


**Fig. 18** Evolution of the  $\sigma/\mu$  ratio (CV factor) of the porosity level as a function of the cross-section angle

Euclidean distance mapping is a tool applied on binary images to produce gray level images where each pixel in the background is assigned a brightness value equal to its distance to the nearest boundary. In such a way, the brightness of each pixel encodes the straight line distance (Euclidean distance) to the nearest point of any boundary. The EDM is constructed following an iterative technique, achieved by successive dilations or erosion of the image, and by successively using the 0 and 1 patterns to limit the square or diamond shaped artifacts and hence to improve the isotropy. Another analysis determines the cumulative distribution of the brightness of the pixels. The slope of this distribution, fitted to the straight line portion of the data in the central 80% of the values is calculated. It represents the inverse of the length between a feature boundary and a randomly chosen pixel belonging to the background. The higher the characteristic length (namely the degree of clustering of the bodies of interest) is, the more clustered are the features within the test plane. As an example, Fig. 20 displays three images constituted by black features and white backgrounds (the number of features, as well as their size, remain identical for the three images), ranging from a nearly isotropic spatial distribution (Fig. 20a) to a highly clustered spatial distribution (Fig. 20c). The contrast was enhanced on the EDMs by applying a LOG filter to the original maps. Figure 21 presents the cumulative distribution of the brightness of the pixels in the background. The characteristic distances, or degrees of clustering of the black features, expressed in this case in pixels, were successively found equal to 29, 69, and 105, from the nearly isotropic distribution to the highly clustered distribution.

As an example, this protocol was applied to digital images of porosity distributed within a copper deposit for several cross-section angles. Figure 22 illustrates two examples of calculated EDMs while Table 1 lists the degrees of clustering that were calculated from fitting of the straight line portions in the 80% of the

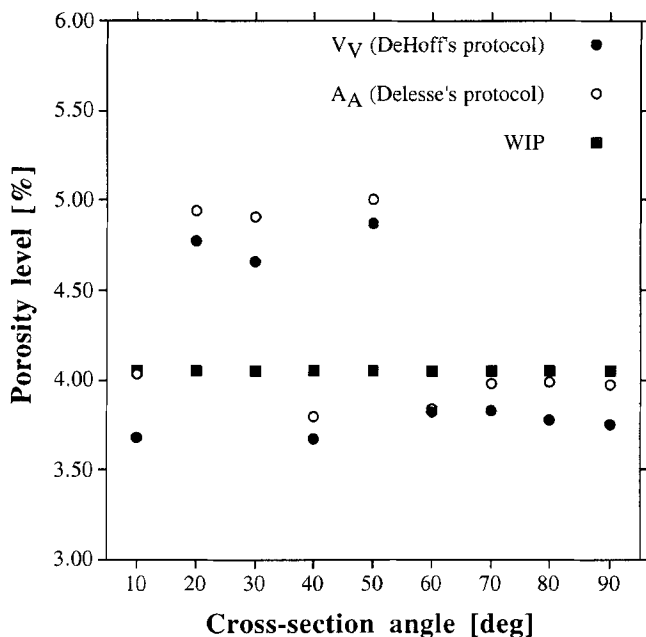


**Fig. 19** Comparison of the porosity data obtained from the DeHoff protocol ( $V_V$ ), the Delesse protocol ( $A_A$ ), and water immersion measurements (WIP)

cumulative distributions of the pixel brightness in the background. The degree of clustering of the porosities remains practically constant whatever the cross-section angle is, indicating a uniform spatial distribution of porosity (the data scatter is equal to 4.7%).

**Table 1** Degrees of clustering of the porosities distributed within a pure copper deposit, for several cross-section angles

Cross-section angle, degrees	Degree of clustering, $\mu\text{m}$
10	12.08
20	11.80
30	12.82
40	13.76
50	13.02
60	12.70
70	13.54
80	12.82
90	13.48

Average value,  $\mu$ , is 12.89  $\mu\text{m}$ . Standard deviation,  $\sigma$ , is 0.61  $\mu\text{m}$ .  $\sigma/\mu$  ratio is 0.047.

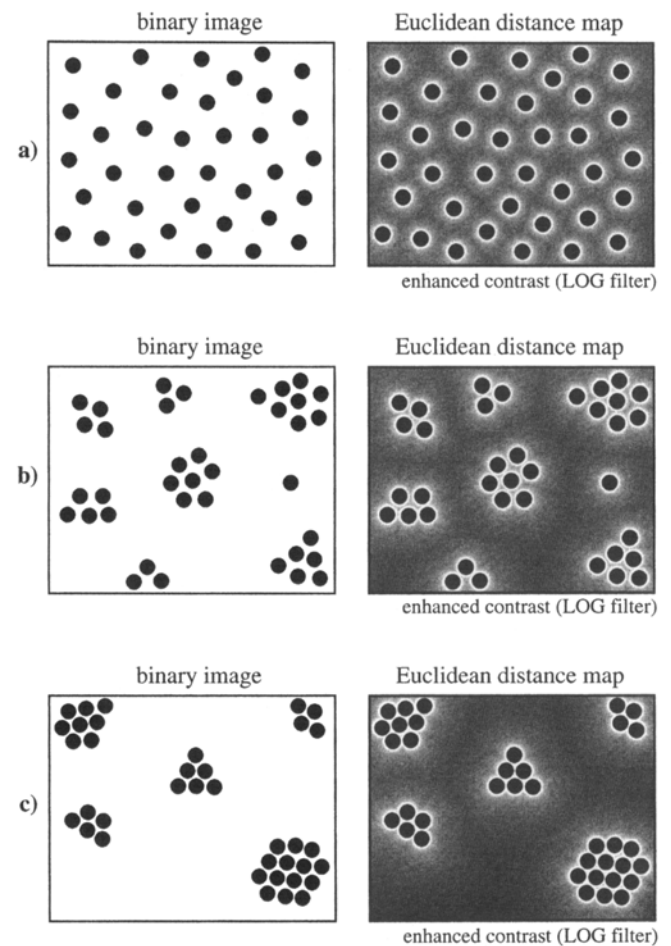


**Fig. 20** Binary images of black features distributed within a white background and corresponding euclidean distance maps. (a) Nearly isotropic spatial distribution. (b) Clustered spatial distribution. (c) Highly clustered spatial distribution

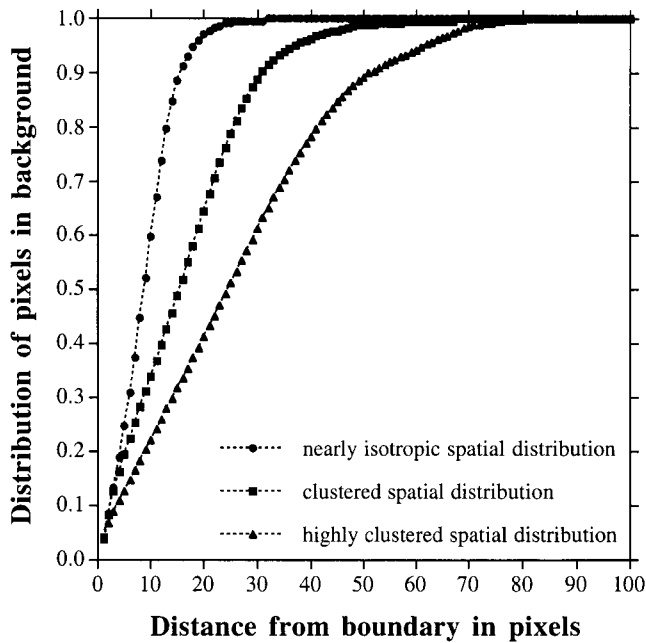


**Fig. 21** Cumulative distribution of the brightness of pixels in the background for the three euclidean distance maps presented in Fig. 18

## 6. Conclusions

Image analysis permits a quantitative description of the microstructural information contained within an image. This approach is well adapted to the quantification of materials microstructures. In the case of thermal spray deposits, this quantification can be applied to the major features of a deposit, such as the flattening degree of particles, the proportion of unmolten particles, the porosity, the oxide content.

The use of a metallographic index, determined by implementing image analysis, is presented. Several macroscopic and structural descriptors, referring to the deposit average thickness, the upper surface fractal dimension, the size-shape distribution of the bodies of interest, and the degree of clustering of these same bodies were described.

## Acknowledgment

The authors thank Paul Carrico, Laurent Mangin, and Crisalia Matheus for their help in the quantitative analysis of the samples. One of the authors (CCB) acknowledges support under NSF DMR 96 32570.

## References

1. G.A. Blann, The Important Role of Microstructural Evaluation in Each Phase of Thermally Sprayed Coatings Application, *Thermal Spray: International Advances in Coatings Technology*, C.C. Berndt and T.F. Bernecki, Ed., ASM International, 1992, p 959-966
2. "Standard Practice for Evaluating Apparent Grain Size and Distribution of Cemented Tungsten Carbides," B 390, *1986 Annual Book of ASTM Standards, Part 2*, ASTM, 1986, p 204-208
3. "Standard Method for Metallographic Determination of Microstructure in Cemented Carbides," B 657, *1986 Annual Book of ASTM Standards, Part 2*, ASTM, 1986, p 557-561

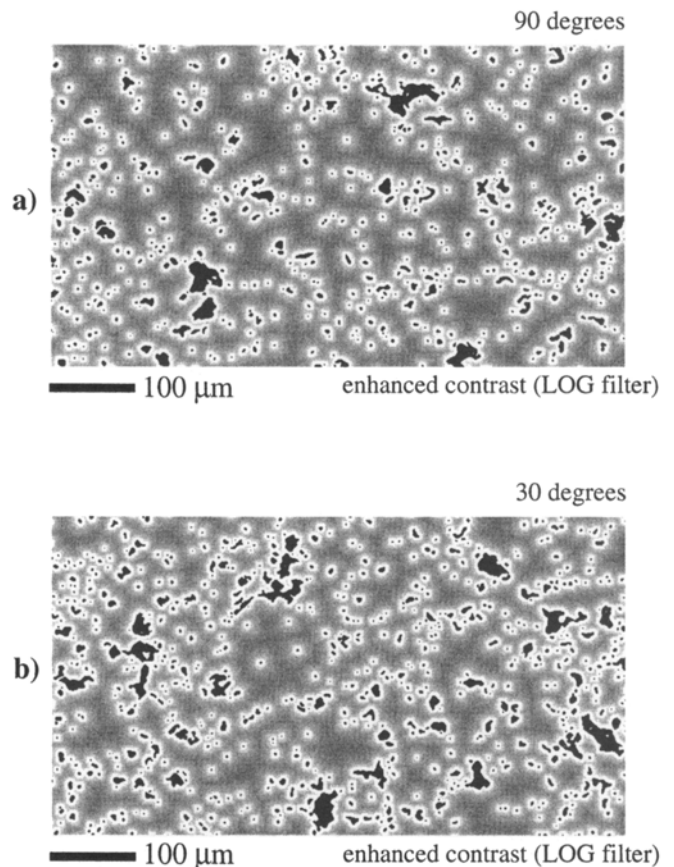


**Fig. 22** Example of Euclidean distance maps of the porosities distributed within a pure copper deposit. (a) For a 90° cross-section angle. (b) For a 30° cross-section angle

4. "Standard Test Methods for Determining Average Grain Size Using Semiautomatic and Automatic Image Analysis," E 1382, *1993 Annual Book of ASTM Standards, Part 3*, ASTM, 1993, p 995-1006
5. "Standard Test Methods for Measurement of Metal and Oxide Coating Thickness by Microscopical Examination of a Cross Section," B 487, *1986 Annual Book of ASTM Standards, Part 2*, ASTM, 1986, p 313-317
6. "Standard Guide for Measurement of Thickness of Metallic and Inorganic Coatings," B 659, *1986 Annual Book of ASTM Standards, Part 2*, ASTM, 1986, p562-565
7. W. Weibull, A Statistical Distribution Function of Wide Applicability, *J. Appl. Mech.*, Vol 18, 19851, p 293-297
8. F.L. Laque and H.R. Copson, *Corrosion Resistance of Metals and Alloys*, 2nd ed., Reinhold Publishing, 1963, 712 pages
9. D. Landolt, *Traité des Matériaux*, Vol 12, *Corrosion et Chimie des Surfaces des Métaux (Treatise on Materials, Vol 12, Corrosion and Chemistry of Metallic Surfaces)*, Presses Polytechniques et Universitaires Romandes, Lausanne, Switzerland, 1993, 552 pages (in French)
10. M.G. Fontana, Materials Science and Engineering Series, *Corrosion Engineering*, 3rd ed., McGraw-Hill, 1986, p 556
11. K.J. Hollis, Pore Phase Mapping, *Thermal Spray: International Advances in Coatings Technology*, C.C. Berndt and T.F. Bernecki, Ed., ASM International, 1992, p 959-966
12. B. Mandelbrot, *Les Objets Fractals, Forme, Hasard et Dimension (The Fractal Objects, Shape, Hazard and Dimension)*, 4th ed., Flammarion, Paris, 1995, 208 pages (in French)



13. J.F. Gouyet, *Physique et Structures Fractales (Physics and Fractal Structures)*, Masson, Paris, 1992, 234 pages (in French)
14. E. Hornbogen, Fractals in Microstructure of Metals, *Int. Mater. Rev.*, Vol 34 (No. 6), 1989, p 277-296
15. M. Coster and J.L. Chermant, Recent Developments in Quantitative Fractography, *Int. Met. Rev.*, Vol 28 (No. 4), 1983, p 228-250
16. B.H. Kaye, Multifractal Description of a Rugged Fineparticle Profile, *Part. Charact.*, Vol 1, 1984, p 14-21
17. K. Wright and B. Karlsson, Fractal Analysis and Stereological Evaluation of Microstructures, *J. Microsc.*, Vol 129 (No. 2), 1983, p 185-200
18. H. Schwarz and H.E. Exner, The Implementation of the Concept of Fractal Dimension on a Semi-Automatic Image Analyzer, *Powder Technol.*, Vol 27, 1980, p 207-213
19. J.C. Russ, *The Image Processing Handbook*, 2nd ed., CRC Press, 1995, p 674
20. R.H. Dauskardt, F. Haubensak, and O. Ritchie, On the Interpretation of the Fractal Character of Fracture Surfaces, *Acta Metall. Mater.*, Vol 38 (No. 2), 1990, p 143-159
21. J.P. Keustermans, Développement de la fractographie fractale pour l'étude de la rupture d'un alliage Zn-Al (Development of the Fractal Fractography for the Study of the Fracture of a Zn-Al Alloy), *Rev. Met.*, Feb 1994, p 323-334 (in French)
22. X. Want, O. Popoola, and R.C. McCune, The Microstructure and Wear Mechanisms of Wire-Arc Sprayed Inconel 625 Coatings on 319 Aluminum, *Thermal Spray Science and Technology*, C.C. Berndt and S. Sampath, Ed., ASM International, 1995, p 633-638
23. S.H. Leigh, C.K. Lin, S. Sampath, H. Herman, and C.C. Berndt, An Elastic Response Method of Testing Thermal Spray Deposits, *Thermal Spraying, Current Status and Future Trends*, A. Ohmori, Ed., High Temperature Society of Japan, Osaka, Japan, 1995, p 945-950
24. E.R. Weibel, *Stereological Methods*, Vol 2, *Theoretical Foundations*, Academic Press, 1980, p 223-311
25. M. Pasandideh-Frad and J. Mostagimi, Deformation and Solidification of Molten Particles on a Substrate in Thermal Plasma Spraying, *Thermal Spray Industrial Applications*, C.C. Berndt and S. Sampath, Ed., ASM International, 1994, p 405-414
26. S.D. Wicksell, the Corpuscule Problem. Second Memoire. Case of Ellipsoidal Corpusculé, *Biometrika*, Vol 18, 1926, p 151-172
27. G.M. Tallis, Estimating the Distribution of Spherical and Elliptical Bodies in Conglomerates from Plane Sections, *Biometrics*, Vol 26, 1970, p 87-103
28. R.T. DeHoff and F.N. Rhines, Determination of Number of Particles per Unit Volume from Measurements Made on Random Plane Sections: The General Cylinder and the Ellipsoid, *Trans. Metall. Soc. AIME*, Vol 221, 1961, p 975-982
29. R.T. DeHoff, The Determination of the Size Distribution of Ellipsoidal Particles from Measurements Made on Random Plane Sections, *Trans. Metall. Soc. AIME*, Vol 224, 1962, p 474-477
30. L.M. Cruz-Orive, Particle Size-Shape Distributions: The General Spheroid Problem. I. Mathematical Model, *J. Microsc.*, Vol 107 (No. 3), 1976, p 235-253
31. L.M. Cruz-Orive, Particle Size-Shape Distributions: The General Spheroid Problem. II. Stochastic Model and Practical Guide, *J. Microsc.*, Vol 112 (No. 2), 1978, p 153-167
32. G. Montavon, S.H. Leigh, C. Coddet, S. Sampath, H. Herman, and C.C. Berndt, Stereological Analysis of Thermally Sprayed Deposits, *Thermal Spray Science and Technology*, C.C. Berndt and S. Sampath, Ed., ASM International, 1995, p 279-283
33. S.H. Leigh, G. Montavon, C. Coddet, S. Sampath, H. Herman, and C.C. Berndt, Quantitative Analysis of Thermal Spray Deposits Using Stereology, *Thermal Spray Science and Technology*, C.C. Berndt and S. Sampath, Ed., ASM International, 1995, p 273-278
34. S.A. Saltykov, The Determination of the Size Distribution of Particles in an Opaque Material from a Measurement of the Size Distribution of Their Sections, *Stereology*, H. Elias, Ed., Springer-Verlag, 1967, p 163-173
35. S. Uematsu, S. Amada, T. Senda, and S. Sato, On Pore Structure of Plasma-Sprayed Films, *Proc. Int. Symposium on Advanced Thermal Spraying Technologies and Allied Coatings*, High Temperature Society of Japan, Osaka, Japan, 1987, p 379-383
36. J. Ilarsky, C.C. Berndt, H. Herman, J. Forman, J. Dubsky, P. Chaska, and K. Neufuss, Analysis of Porosity of Free-Standing Ceramics Manufactured by Plasma Spraying, *Thermal Spray Coatings: Research, Design and Applications*, C.C. Berndt and T.F. Bernecki, Ed., ASM International, 1993, p 575-579
37. J.L. Chermant, Analyse d'images et morphologie mathématique: une introduction, (Image Analysis and Morphological Mathematics: an Introduction), *Rev. Met.*, Feb 1994, p 201-209 (in French)
38. "Standard Test Methods for Density and Interconnected Porosity of Sintered Powder Metal Structural Parts and Oil-Impregnated Bearings," *1986 Annual Book of ASTM Standards, Part 2*, ASTM, 1986, p 163-164
39. S. Boire-Lavigne, C. Moreau, and R.G. Saint-Jacques, The Relationship between the Microstructure and Thermal Diffusivity of Plasma-Sprayed Tungsten Coatings, *J. Thermal Spray Technol.*, Vol 4 (No. 3), 1995, p 261-267
40. J.G.C. Wolke, J.M.A. de Blik-Hogervorst, and W.J.A. Dhert, Studies on the Thermal Spraying of Apatite Bioceramics, *J. Thermal Spray Technol.*, Vol 1 (No. 1), 1992, p 75-82
41. K.A. Khor and P. Cheang, Characterization of Thermal Sprayed Hydroxyapatite Powders and Coatings, *J. Thermal Spray Technol.*, Vol 3 (No. 1), 1994, p 45-50